Research Square

Preprints are preliminary reports that have not undergone peer review.
They should not be considered conclusive, used to inform clinical practice,
or referenced by the media as validated information.

Mode-Dependent Failure Behaviour of GFRP Laminates Containing Mid-Plane PTFE Delaminations: A Modified Arcan Investigation

Abdul Mateen Mohammed

abdulmateen7@gmail.com

CMR University https://orcid.org/0000-0002-4666-4465

A. Kiran Kumar

TKR College of Engineering and Technology

Arun Kumar K. H

CMR University

Case Report

Keywords: GFRP, Modified Arcan test, Mode-dependent failure, Mid-plane delamination, PTFE insert, Mixed-mode loading, Failure envelope

Posted Date: May 28th, 2026

DOI: https://doi.org/10.21203/rs.3.rs-9816622/v1

License: This work is licensed under a Creative Commons Attribution 4.0 International License.
Read Full License

Additional Declarations: The authors declare no competing interests.

Abstract

Mid-plane delaminations are a common defect in GFRP laminates. They arise during manufacturing or in service, and their growth under combined opening and shear loading governs the residual life of the structure. In this study, woven E-glass/Lapox L-12 epoxy butterfly specimens were prepared with pre-implanted polytetrafluoroethylene (PTFE) delaminations of three shapes (circular, elliptical, square) and three nominal areas (60, 80, 100 mm^2) and tested in a modified Arcan fixture. Each specimen was loaded at one of three angles: pure Mode-I (0°), mixed mode (45°), and pure Mode-II (90°). The apparent failure stress at the ligament dropped by about 65% from Mode-I to Mode-II, while the apparent specific failure energy remained nearly constant across the three modes. This mode-invariance of the energy metric reflects a roughly 50-fold rise in the toe-corrected initial compliance over the same range of loading angles. Within each plate, the spread of apparent failure stress across the three defect shapes at a fixed loading angle was 8 to 12%, which is comparable to single-specimen scatter for GFRP shear tests reported in the literature. Because every tested defect fully spans the 6 mm ligament, the apparent shape and area effects are interpreted as variations in the geometry of the delamination boundary at the V-notch flanks rather than as size effects at the failure plane. The reported values are apparent stresses specific to this fixture and geometry and should not be interpreted as intrinsic material properties.

1. Introduction

GFRP composites are used in aerospace, marine, automotive, wind-energy, and civil applications because of their specific strength, corrosion resistance, and design flexibility [1–3]. The most common failure mode in laminated composites is delamination, the separation of adjacent plies. Delamination can develop without surface evidence and still reduce the compressive strength, stiffness, and fatigue life of the structure [4, 5].

Delaminations originate from manufacturing defects such as voids, resin-rich pockets, and foreign-body inclusions, or from in-service events such as low-velocity impact, edge stresses, and machining damage [6, 7, 22]. The local loading at a delamination is rarely pure opening or pure shear; most realistic loads produce a mixture of the two. The fracture energy required to advance a delamination depends on this mode mixity. It is conventionally measured using the Double Cantilever Beam (DCB) test for pure Mode-I [8], the End-Notched Flexure (ENF) test for pure Mode-II [9], and the Mixed-Mode Bending (MMB) test for combined loading [10]. Non-destructive and inverse approaches, such as vibration-based delamination assessment, have also been reported [24].

The modified Arcan test offers an alternative route to combined-loading characterisation. The original butterfly specimen, proposed by Arcan, Hashin, and Voloshin [11, 14], is loaded through a circular fixture. Rotating the fixture relative to the V-notch axis varies the ratio of normal to shear stress at the ligament continuously, from pure tension at 0° to pure shear at 90°. A single specimen geometry can therefore cover the full mode-mixity range without reconfiguration. El-Hajjar and Haj-Ali [12] refined the butterfly geometry for thick-section pultruded FRP composites and showed by finite-element analysis that the

gauge region is in nearly uniform shear at 90° loading. Later studies have applied the technique to pure shear and combined normal/shear characterisation of fibre composites [13] and to failure prediction in hybrid composite systems [15]. Comparable mode-dependent damage features have been reported for notched CFRP under multi-axial loading [23].

Most modified Arcan studies on composites have either used undamaged specimens or fixed the defect type and varied only the loading angle. Few have systematically varied both defect shape and defect area together with mode mixity for laminates containing embedded delaminations. The present study addresses this gap. Butterfly specimens were prepared from woven E-glass/epoxy with mid-plane delaminations seeded by 80 μm PTFE film of three shapes (circular, elliptical, square) and three nominal areas (60, 80, 100 mm^2). Each specimen was tested at one of three loading angles (0°, 45°, 90°). PTFE film is the standard release material for seeding artificial delaminations in fracture studies because cured epoxy does not bond to it [10, 16].

The goals of this study are (i) to characterise the apparent ligament failure stress as a function of mode mixity and defect geometry, and (ii) to compare stress-based and energy-based metrics for ranking failure susceptibility. One geometric constraint must be flagged at the outset: the mid-plane delamination of every defect specimen exceeds the 6 mm ligament width.

2. Materials and Methods

2.1 Materials

The reinforcement is a bidirectional woven E-glass fabric of 10-mil weave with a nominal ply thickness of 0.254 mm; the warp and weft directions are taken as 0° and 90° respectively. The matrix is a commercial low-viscosity DGEBA-type epoxy resin (Lapox L-12) with K-6 amine hardener, supplied by Atul Ltd., India. The resin and hardener were mixed at the manufacturer-specified ratio and applied to the reinforcement. The laminates were consolidated by compression moulding and cured at room temperature. An 80 μm polytetrafluoroethylene (PTFE) film was used as the defect-seeding insert.

2.2 Laminate Fabrication

Four laminates were fabricated by hand layup: one virgin (no defect) reference plate, and three defect-bearing plates corresponding to nominal defect areas of 60, 80, and 100 mm^2. Each plate contained 12 plies of woven E-glass. For the defect-bearing plates, a single piece of PTFE film of the appropriate shape and area was placed at the mid-plane (between plies 6 and 7) before consolidation. Within each defect-bearing plate, three defect shapes were positioned at the locations from which individual specimens were later cut: circular (diameter calculated from the target area), elliptical (major-to-minor axis ratio of 2:1, major axis aligned with the future ligament line), and square (edges parallel to the future ligament line). After resin impregnation, each plate was consolidated under hand pressure and cured at room temperature. All specimens within a given defect-area family (for example, the nine specimens

from the 60 mm^2 plate) were cut from the same plate; cross-plate comparisons are therefore not reported quantitatively.

2.3 Specimen Geometry

The geometric details of the butterfly specimens are given in Fig. 1. The total planform size of the butterfly specimens was 96 × 80 mm and consisted of two symmetric V-shaped notches with the help of which the central ligament was created with a size of 6 mm. Six holes of 10 mm size (three on each side) carried the load through the modified arcan fixture. The flanks of the notches had an angle of 90°. The specimens were cut from the composite plates by water jet technique to avoid heating at notch tips.

2.4 Defect Configurations and Test Matrix

As there are three defect shapes, three defect areas and three loading angles the full test matrix contains of 30 nominal configurations, plus three virgin baselines. The specific defect dimensions for each target area are listed in Table 1.

Table 1
Defect characteristic dimensions for each target area.

Target area (mm^2)	Circle diameter (mm)	Square side (mm)	Ellipse 2*a* × 2*b* (mm)
60	8.74	7.75	12.36 × 6.18
80	10.09	8.94	14.28 × 7.14
100	11.28	10.00	15.96 × 7.98

The applied load was directed at three angles relative to the ligament: 0° (load normal to the ligament, pure Mode-I), 45° (mixed Mode-I/II), and 90° (load parallel to the ligament, pure Mode-II). Under this convention, the applied load F decomposes into a ligament normal stress $\sigma_n = F\cos(\theta) / A_l$ and a ligament shear stress $\tau = F\sin(\theta) / A_l$, where A_l = 6 mm × thickness is the ligament cross-section.

Specimens are designated by the format (area-code)-A-(shape)-(angle-code), where the area-code is 6, 8, or 10 (for 60, 80, and 100 mm^2), the shape is C, E, or S (for Circle, Ellipse, or Square), and the angle-code is 0, 4, or 9 (for 0°, 45°, and 90°). Virgin specimens are designated AV0, AV4, and AV9. For example, 8AC4 is an 80 mm^2 circular-defect specimen tested at 45°.

2.5 Test Procedure

Tests were carried out at on a universal testing machine fitted with a modified Arcan fixture. Load was applied through six bolts in the 10 mm holes. The fixture was rotated to the specified angle and locked before each test. The crosshead speed was 5 mm/min for all specimens. Load and crosshead displacement were recorded continuously up to specimen failure. The maximum load F_{max} and the corresponding extension were extracted from each load–displacement curve.

2.6 Data Analysis

The apparent ligament failure stress was computed as $\sigma_{app} = F_{max} / A_l$, and decomposed into $\sigma_n = F_{max} \cos(\theta) / A_l$ and $\tau = F_{max} \sin(\theta) / A_l$. All curves showed a toe region of about 1–2 mm at the beginning of the load-displacement response, due to clearances in the bolt holes and at the clamps. The toe region was corrected before analyzing the compliance and energy. The line that gave the largest tangent value within the first 10%-to-50% of Fmax was extrapolated backwards to F = 0, and the corresponding x-intercept point (1.19, 1.62, and 1.47 mm for 0°, 45°, and 90° loading, respectively) was subtracted from all displacements. The initial compliance coefficient C0 was calculated using linear least squares regression for the toe-corrected data points between 10% and 30% of Fmax. Strain energy at failure was calculated by Uf = ∫F dδ between the new origin and Fmax using the trapezoidal rule.

Specific failure energy was defined as Gapp = Uf / (t · a0), where t is the thickness of the specimen, and a0 is a characteristic delamination half-length: radius of a circle, semi-major axis along the ligament line for an ellipse, and one-half of the side length for a square geometry. For unaged specimens, a0 = 3 mm (the half-width of the ligament). Mode components are GI,app = Gapp cos²θ and GII,app = Gapp sin²θ. Note that Gapp ≠ GIc for the material (interlaminar fracture toughness), since Uf includes both the interfacial strain energy and the bulk elastic strain energy.

3. Results

3.1 Load–Displacement Behaviour

Figure 2 shows the load-displacement graphs for all the three plates having defects at three different loading angles. The shape of the graph for a certain angle remains constant among all the three plates, where the graph exhibits the same behavior for the area of defects 60, 80, and 100 square mm. The change in response with loading angle dominates any within-plate variation. At 0° loading (Mode-I), all three shapes in each plate produce a nearly linear response up to about 8–10 kN, followed by a brittle drop at peak. At 45° (mixed mode), the response remains close to linear, but the peak load drops to about 5.5–7 kN at roughly twice the corrected displacement. At 90° (Mode-II), the curves rise slowly and sub-linearly to a much lower peak (about 3–3.8 kN) at corrected displacements of 13–17 mm. The growth in compliance with loading angle is the dominant effect. Specimen 8AC0 (80 mm^2 circle at 0°) was lost during fabrication and is therefore absent from the corresponding cell.

3.2 Failure Loads and Stresses

Table 2 summarises the maximum load, ligament cross-sectional area, and decomposed normal and shear stresses at failure for the 28 successfully tested specimens. F_{max} ranged from 3,098 N (AV9) to 10,650 N (10AE0). σ_{app} ranged from approximately 197 MPa (AV9) to 792 MPa (10AE0).

Table 2
Test results: maximum load and decomposed stresses at the ligament cross-section. Specimen 8AC0 (80 mm² circle at 0°) was lost during fabrication.

Specimen	Shape	Area (mm^2)	Angle θ (°)	Thickness t (mm)	F_{max} (N)	σ_{app} (MPa)	σ_n (MPa)	τ (MPa)
AV0	—	0	0	2.70	8649	533.9	533.9	0
AV4	—	0	45	2.30	5629	411.5	290.9	290.9
AV9	—	0	90	2.60	3098	197.1	0	197.1
6AC0	Circle	60	0	2.30	9358	690.1	690.1	0
6AC4*	Circle	60	45	2.20	6562	503.9	356.4	356.4
6AC9	Circle	60	90	2.20	3131	237.2	0	237.2
6AE0	Ellipse	60	0	2.30	8738	641.5	641.5	0
6AE4	Ellipse	60	45	2.30	5452	403.8	285.5	285.5
6AE9	Ellipse	60	90	2.30	3371	249.7	0	249.7
6AS0	Square	60	0	2.10	9192	712.5	712.5	0
6AS4	Square	60	45	2.20	6213	468.5	331.3	331.3
6AS9	Square	60	90	2.30	3676	267.5	0	267.5
8AC4	Circle	80	45	2.20	6966	525.3	371.4	371.4
8AC9	Circle	80	90	2.40	3286	225.4	0	225.4
8AE0	Ellipse	80	0	2.20	10007	772.1	772.1	0
8AE4	Ellipse	80	45	2.10	6267	499.8	353.4	353.4
8AE9	Ellipse	80	90	2.10	3170	248.0	0	248.0
8AS0	Square	80	0	2.30	9741	715.2	715.2	0
8AS4	Square	80	45	2.20	6426	495.9	350.6	350.6
8AS9	Square	80	90	2.30	3430	244.3	0	244.3
10AC0	Circle	100	0	2.20	9730	727.2	727.2	0
10AC4	Circle	100	45	2.10	5889	458.6	324.3	324.3
10AC9	Circle	100	90	2.20	3485	267.7	0	267.7
10AE0	Ellipse	100	0	2.20	10650	792.4	792.4	0
10AE4	Ellipse	100	45	2.30	6637	472.8	334.3	334.3
10AE9	Ellipse	100	90	2.30	3783	277.7	0	277.7

Specimen	Shape	Area (mm^2)	Angle θ (°)	Thickness t (mm)	F_{max} (N)	σ_{app} (MPa)	σ_n (MPa)	τ (MPa)
10AS0	Square	100	0	2.10	9774	768.4	768.4	0
10AS4	Square	100	45	2.10	6190	486.6	344.1	344.1
10AS9	Square	100	90	2.10	3670	291.3	0	291.3

** Specimen 6AC4 failed by net-tension fracture at the upper bolt grip rather than at the ligament.*

3.3 Failure Envelope

Figure 3 shows the σn-τ values for each plate and the two envelopes superimposed on them. The linear (Mohr-Coulomb) and the quadratic (Tsai-Hill) envelopes are defined by the equations σn/X + τ/S = 1 and (σn/X)2 + (τ/S)2 = 1, respectively, and intersect at identical points in the pure-mode regime. Note that X here is the mean normal stress σn at 0° loading and S is the mean shear stress τ at 90° loading. Specimen 6AC4 is disregarded (see Section 4.3).

The values at the 45° angle deviate from both envelopes in every plate considered. Taking an average value of σn/X + τ/S at 45° gives us a value of 1.78, which exceeds the expected one from the linear envelope of 1.0 by a factor of 1.78, while the corresponding value for (σn/X)2 + (τ/S)2 is 1.95. Thus, both the standard envelopes underestimate the critical failure stress in mixed mode conditions by a factor of almost two. This shift of the critical point occurs for all the plates, implying a physical effect rather than noise in experimental values.

A possible physical explanation for the above is the activation of both fibre fracture and matrix shear simultaneously by the applied mixed-mode loading. Pure Mode-I induces fibre fracture, while Pure Mode-II induces matrix shear. Since both phenomena happen at once, it takes more force to activate them together than is expected when simply adding up the required forces for each mode separately.The fractography in Fig. 7 is consistent with this picture. The 45° specimens show damage zones intermediate between the narrow Mode-I cracks and the wide Mode-II broomed regions, and the same fracture surface carries visible fibre rupture and matrix shear.

The lump-sum stress decomposition $\sigma_n = F\cos(\theta)/A$ and $\tau = F\sin(\theta)/A$ is also relevant. These are engineering averages over the ligament cross-section, not local stresses at the V-notch tips, where singular and constraint contributions scale with loading angle differently from the ligament average. A finite-element analysis of the local stress state at the notch tip would help clarify how much of the apparent envelope concavity arises from real mechanism interaction and how much is an artefact of the F/A approximation.

We do not claim a specific failure criterion from three loading angles. Three angles are the minimum needed to detect non-monotonic envelope behaviour but not enough to fit a curve. The departure of the 45° points from standard criteria is reported here as an exploratory observation. Resolving it would

require additional loading angles between 0° and 90°, with replicates at each angle, together with finite-element calibration of the local stress state at the notch tip.

3.4 Effect of Loading Angle

Figure 4 plots σ_{app} against loading angle, separately for each defect plate. Within every plate, σ_{app} falls monotonically from 0° to 90°. The mean ratio $\sigma_{app}(0°)/\sigma_{app}(90°)$ over the nine defect configurations is 2.84, so pure Mode-II loading reduces the ligament stress to about 35% of the pure Mode-I value. The 45° mixed-mode value is about 65% of the Mode-I value and sits on a near-linear path between the two pure modes.

3.5 Effect of Defect Shape and Area

Within each plate, the spread of σ_{app} across the three defect shapes at a given loading angle is 8 to 12% of the within-plate mean. At Mode-I in the 60 mm^2 plate, σ_{app} values were 690 MPa (Circle), 642 MPa (Ellipse), and 713 MPa (Square), spanning 71 MPa, or 10.5% of the mean. The shape ranking is not consistent across plates: Square is highest at Mode-I in the 60 mm^2 plate, while Ellipse is highest at Mode-I in the 80 and 100 mm^2 plates.

3.6 Compliance and Energy

Figure 5 shows the toe-corrected initial compliance C_0 for all specimens on a logarithmic axis. The mean C_0 rises from about 0.78×10^{-3} mm/N at Mode-I to about 41×10^{-3} mm/N at Mode-II, a factor of about 50. The apparent specific failure energy G_{app}, by contrast, is nearly invariant with loading angle. Figure 6 compares the angle dependence of σ_{app} and G_{app}, both normalised to their Mode-I values. While σ_{app} falls to 0.35 at Mode-II, G_{app} stays within ± 21% of its Mode-I value, with a slight peak at 45°.

3.7 Failure Modes

The figure below shows the nine specimens that were obtained as a result of the failure from the 60 mm2 plate (Fig. 7). Failure development in all three notches remains uniform for all variations in angles. In the case of an angle of 0° (Mode I, left column), failure happens without much damage to the fibers. Here, failure results into a thin almost opaque band in the ligament with little matrix cracks on the flanks of the V-notch. For the 45° angle (mixed mode, center column), failure surface becomes wider with fiber pull-out at the end of the ligament becoming obvious. With the angle 90° (Mode II, right column), failure involves large brush and broom of fibers beyond the ligament length of 6mm. Extensive fiber pull-out together with matrix shear is evident. An exception occurs in one specimen, where specimen 6AC4 (mixed mode, circular notch) fails at the top bolt holes indicating failure due to bearing.

4. Discussion

4.1 Mode-Dependent Failure Stress

The apparent failure stress drops by a factor of about 2.84 from Mode-I to Mode-II. This is broadly consistent with the mode dependence reported in the GFRP literature. Under Mode-I, the ligament is pulled in tension across its axis. For a 0/90 woven E-glass laminate, this direction is parallel to one set of fibres, so the ligament fails through a combination of fibre tensile rupture and matrix tension. Under Mode-II, the ligament is sheared along its axis, and failure is dominated by matrix shear. Matrix shear is weaker than fibre tension because the cured epoxy has a lower shear strength than the glass fibres have in tension. The 45° mixed-mode case applies equal normal and shear components, and the failure stress lies between the two extremes.

The σ_{app} values reported here (530 to 790 MPa at Mode-I; 200 to 290 MPa at Mode-II) are higher than what is typically reported for unconstrained tensile or shear specimens in similar GFRP systems [18, 19]. The deep V-notches and the short 6 mm ligament constrain the failure region. This constraint produces a triaxial stress state at the failure plane and raises the apparent stress above the unconstrained material strength. The values reported here should therefore be read as apparent stresses specific to this fixture and geometry, not as intrinsic material properties.

4.2 Mode-Invariance of Apparent Specific Failure Energy

The apparent specific failure energy G_{app} is nearly invariant across the three loading modes, despite the large drop in σ_{app}. The mechanism is visible in the compliance behaviour. The roughly 50-fold rise in toe-corrected C_0 from Mode-I to Mode-II shows that the specimen becomes much more deformable under shear-dominated loading. Higher compliance means greater displacement at failure, and therefore greater integrated work, even though the peak load itself is smaller. The product $F^2 \cdot C_0$ stays comparable across loading angles, and U_f and G_{app} stay comparable along with it.

One reading is that the laminate has a roughly mode-independent total energy capacity, while the partition of that capacity between high stress at small displacement (Mode-I) and lower stress at larger displacement (Mode-II) is mode-dependent. The slight peak in G_{app} at 45° (about 21% above Mode-I) may reflect simultaneous activation of both opening and shear mechanisms in the mixed condition. This is offered as a hypothesis-level reading given the n = 1 design, and would require verification with replicate testing and detailed fractography.

G_{app} is not equivalent to the interlaminar fracture toughness G_{Ic} of the laminate. The integrated U_f includes the bulk elastic strain energy stored throughout the specimen prior to failure, most of which is not released into the delamination front. The G_{app} values reported (2,400 to 6,100 kJ/m^2) are accordingly several orders of magnitude larger than literature G_{Ic} values for glass/epoxy systems (about 0.2 to 0.5 kJ/m^2) [16, 17]. G_{app} is used here only as a relative comparative metric.

4.3 Failure Modes and Mechanism Inference

The fractographic record in Fig. 7 supports the energy interpretation above. At 0°, the failure surface is narrow and shows little fibre disturbance, consistent with brittle tensile rupture at small displacement: high stress, low absorbed energy density, narrow damage zone. At 90°, the failure surface is wide and shows extensive fibre brooming, consistent with progressive matrix shear and fibre pull-out: low stress, large displacement, wide damage zone. The 45° specimens fall between these limits in damage extent, consistent with the intermediate σ_{app} and the slight peak in G_{app} at this angle. The visible widening of the damage zone with loading angle is the fractographic correlate of the rise in C_0 in Fig. 5: more deformable behaviour at 90° produces a larger volume of damaged material before peak load. Comparable mode-dependent damage features have been reported for notched CFRP under multi-axial loading [23].

Specimen 6AC4 failed by net-tension fracture at the upper bolt grip rather than at the ligament. The recorded peak load of 6,562 N for this specimen represents the bearing capacity of the bolt-loaded grip, not the mixed-mode failure capacity of the ligament. We exclude 6AC4 from quantitative within-plate shape comparisons but retain it in Table 2 for completeness, marked with an asterisk. The single occurrence of this failure mode in 28 tests is consistent with reports in the modified Arcan literature [12, 13] and indicates that bolt-bearing failure is a low-frequency competing failure mode for this specimen geometry. Loading-bolt design improvements, such as a longer bolt-to-edge distance, larger washers, or a higher-strength laminate in the grip region, would mitigate this in future testing.

4.4 Defect Shape and Size Effects

Within each plate, the spread of σ_{app} across the three defect shapes at fixed loading angle is 8 to 12%. This is comparable to the single-specimen scatter reported for replicate GFRP shear tests in the literature [18, 19]. The shape ranking does not hold consistently across plates, which suggests that the apparent shape effect is at or below the level of $n = 1$ scatter and cannot be statistically separated from random variation in the present dataset. Definitive quantification of shape effects would require replicate testing, typically $n \geq 5$ per condition per ASTM D5379 [20] or ASTM D7078 [21].

A geometric constraint further conditions this interpretation. Even the smallest tested defect (60 mm^2 circle, diameter 8.74 mm) is larger than the 6 mm ligament. In every defect specimen, the PTFE film fully spans the ligament cross-section, so the failure plane is fully pre-delaminated regardless of nominal defect shape or area. The variable that actually changes across configurations is not the size of the embedded defect at the failure plane (which is constant at full ligament coverage), but the extent and curvature of the delamination boundary as it intersects the V-notch flanks. The observed shape effect should therefore be read as a variation in this boundary geometry rather than as a size effect at the failure plane.

4.5 Compliance and Fixture Considerations

The ratio of C_0 from Mode-I to Mode-II is substantially larger than the typical ratio of in-plane shear compliance to in-plane tensile compliance for woven 0/90 E-glass laminates, which is 5 to 10 for similar systems. The remaining excess compliance recorded in the Mode-II tests is plausibly attributable to bolt

clearance and pin-bearing deformation that operate during the steady-state loading phase, not only the initial seating phase. Strain measurements made directly on the specimen surface, for example by digital image correlation, would be needed to separate true material compliance from residual fixture compliance.

5. Conclusions

A modified Arcan investigation of GFRP butterfly specimens with mid-plane PTFE delaminations of three shapes (Circle, Ellipse, Square) and three areas (60, 80, 100 mm^2) was carried out at three loading angles (0°, 45°, 90°). The main findings are as follows:

- The apparent failure stress at the ligament drops monotonically by about 65% from Mode-I to Mode-II, with $\sigma_{app}(0°)/\sigma_{app}(90°) \approx 2.84$ averaged across the nine defect configurations.
- The apparent specific failure energy G_{app} is nearly invariant across loading modes, with a slight peak at 45°. This mode-invariance reflects a roughly 50-fold rise in toe-corrected initial compliance C_0 from Mode-I to Mode-II, which compensates for the drop in peak load.
- Failure modes change visibly with loading angle. Mode-I failures are narrow and dominated by matrix cracking; Mode-II failures are wide and dominated by fibre pull-out and matrix shear; mixed-mode failures fall between the two in damage extent.
- Within each plate, the spread of σ_{app} across the three defect shapes at fixed loading angle is 8 to 12%, comparable to the single-specimen scatter reported for GFRP shear testing. No shape ranking holds consistently across the three plates. Because every tested defect fully spans the 6 mm ligament, the observed shape effect should be interpreted as a variation in the geometry of the delamination boundary at the V-notch flanks rather than as a size effect at the failure plane.
- Linear (Mohr–Coulomb) and quadratic (Tsai–Hill) failure criteria, anchored at the pure-mode endpoints, do not fit the data. The 45° mixed-mode points lie outside both envelopes in every plate, by about 78% for the linear form and 95% for the quadratic. The mixed-mode failure stress is roughly twice what either pure-mode-anchored criterion would predict. The consistency of this offset across three plates suggests a structural effect rather than scatter. Identifying the correct combined-failure criterion would require testing at additional loading angles with replicates, together with finite-element calibration of the local notch-tip stress state.
- The σ_{app} values reported are apparent stresses specific to this fixture and geometry and should not be interpreted as intrinsic material strengths. G_{app} is reported only as a relative comparative metric and is several orders of magnitude larger than literature G_{Ic} values for glass/epoxy systems.
- Future work should include replicate testing at multiple loading angles, direct strain measurement (for example by digital image correlation) to separate material compliance from fixture compliance, and finite-element calibration of the specimen for mode-resolved interlaminar fracture toughness.

References

1. Mallick PK (2007) Fiber-Reinforced Composites: Materials, Manufacturing, and Design, 3rd edn. CRC, Boca Raton, FL, USA
2. Gibson RF (2016) Principles of Composite Material Mechanics, 4th edn. CRC, Boca Raton, FL, USA
3. Soutis C (2005) Fibre reinforced composites in aircraft construction. Prog Aerosp Sci 41(2):143–151
4. Bolotin VV (1996) Delaminations in composite structures: its origin, buckling, growth and stability. Compos Part B: Eng 27(2):129–145
5. Tay TE (2003) Characterization and analysis of delamination fracture in composites: An overview of developments from 1990 to 2001, Applied Mechanics Reviews, vol. 56, no. 1, pp. 1–32
6. Shyr T-W, Pan Y-H (2003) Impact resistance and damage characteristics of composite laminates. Compos Struct 62(2):193–203
7. Khashaba UA (2013) Drilling of polymer matrix composites: A review. J Compos Mater 47(15):1817–1832
8. ASTM D5528-21 (2021) Standard Test Method for Mode I Interlaminar Fracture Toughness of Unidirectional Fiber-Reinforced Polymer Matrix Composites. ASTM International, West Conshohocken, PA
9. ASTM D7905/D7905M-19 (2019) Standard Test Method for Determination of the Mode II Interlaminar Fracture Toughness of Unidirectional Fiber-Reinforced Polymer Matrix Composites. ASTM International, West Conshohocken, PA
10. ASTM D6671/D6671M-22 (2022) Standard Test Method for Mixed Mode I-Mode II Interlaminar Fracture Toughness of Unidirectional Fiber Reinforced Polymer Matrix Composites. ASTM International, West Conshohocken, PA
11. Arcan M, Hashin Z, Voloshin A (1978) A method to produce uniform plane-stress states with applications to fiber-reinforced materials. Exp Mech 18(4):141–146. https://doi.org/10.1007/BF02324146
12. El-Hajjar R, Haj-Ali R (2004) In-plane shear testing of thick-section pultruded FRP composites using a modified Arcan fixture, Composites Part B: Engineering, vol. 35, no. 5, pp. 421–428
13. Banks-Sills L, Arcan M, Bortman Y (1984) A mixed-mode fracture specimen for Mode II dominant deformation. Eng Fract Mech 20(1):145–157
14. Voloshin A, Arcan M (1980) Failure of unidirectional fiber-reinforced materials – New methodology and results, Experimental Mechanics, vol. 20, no. 8, pp. 280–284
15. De Junior S, Gouveia RR, Ito JR, N. M., and dos, Santos DJ (2017) Failure prediction of hybrid composite using Arcan's device and Drucker–Prager model, Polymer Testing, vol. 58, pp. 256–261
16. Davies P, Blackman BRK, Brunner AJ (1998) Standard test methods for delamination resistance of composite materials: current status. Appl Compos Mater 5(6):345–364
17. Sela N, Ishai O (1989) Interlaminar fracture toughness and toughening of laminated composite materials: a review, Composites, vol. 20, no. 5, pp. 423–435

18. Adams DF, Walrath DE (1987) Current status of the Iosipescu shear test method. J Compos Mater 21(6):494–507
19. Pierron F, Vautrin A (1996) The 10° off-axis tensile test: A critical approach. Compos Sci Technol 56(4):483–488
20. ASTM D5379/D5379M-19 (2019) Standard Test Method for Shear Properties of Composite Materials by the V-Notched Beam Method. ASTM International, West Conshohocken, PA
21. ASTM D7078/D7078M-20 (2020) Standard Test Method for Shear Properties of Composite Materials by V-Notched Rail Shear Method. ASTM International, West Conshohocken, PA
22. Janakiraman A, Pemmasani S, Sheth S et al (2020) Experimental investigation and parametric optimization on hole quality assessment during drilling of CFRP/GFRP/Al stacks. J Institution Eng (India): Ser C 101(2):291–302. https://doi.org/10.1007/s40032-020-00563-w
23. Tan JLY, Deshpande VS, Fleck NA (2015) Failure mechanisms of a notched CFRP laminate under multi-axial loading. Compos Part A: Appl Sci Manufac 77:56–66
24. Sreekanth TG, Senthilkumar M, Manikanta Reddy S (2021) Vibration-based delamination evaluation in GFRP composite beams using ANN, Polymers and Polymer Composites, vol. 29, no. 9_suppl, pp. S317–S327. https://doi.org/10.1177/09673911211003399

Figures

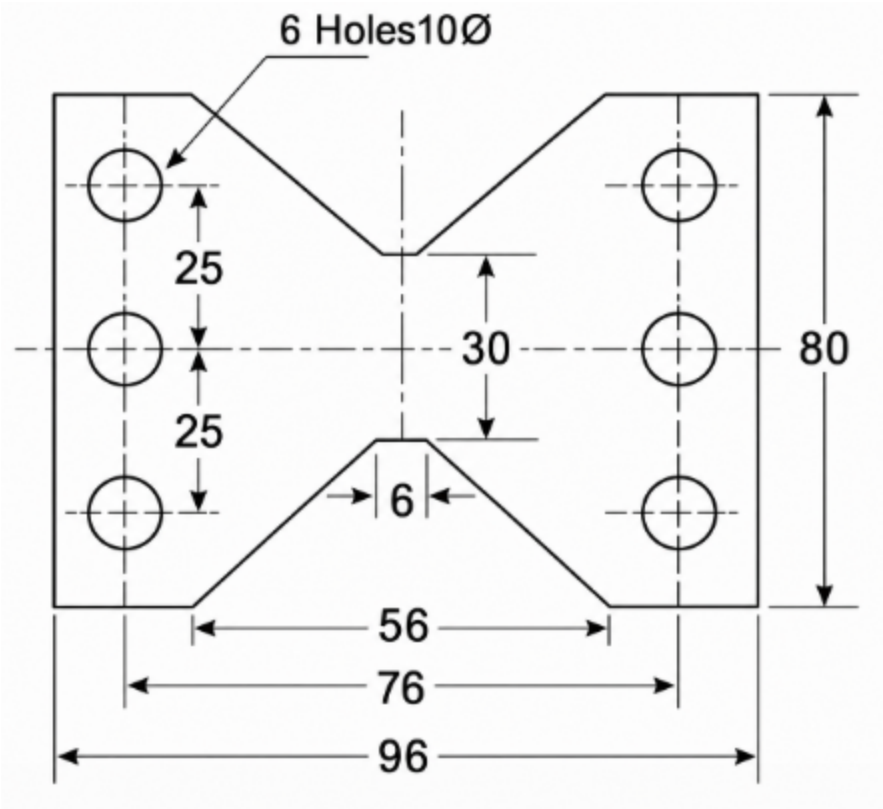


Figure 1

Modified Arcan butterfly specimen. All dimensions in mm.

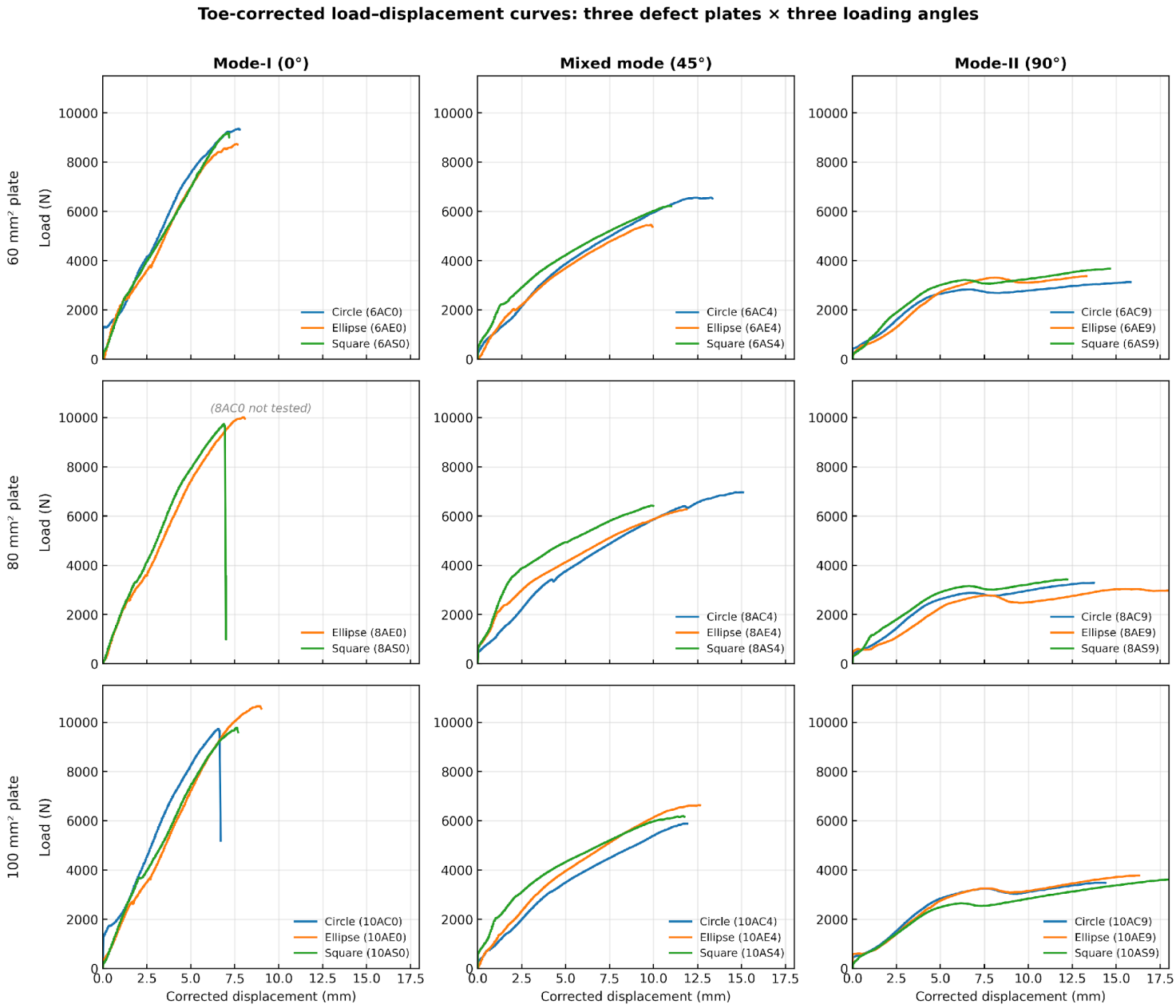


Figure 2

Toe-corrected load–displacement curves for all three defect plates at the three loading angles. Rows: defect plate (60, 80, 100 mm²). Columns: loading angle (Mode-I 0°, mixed 45°, Mode-II 90°).

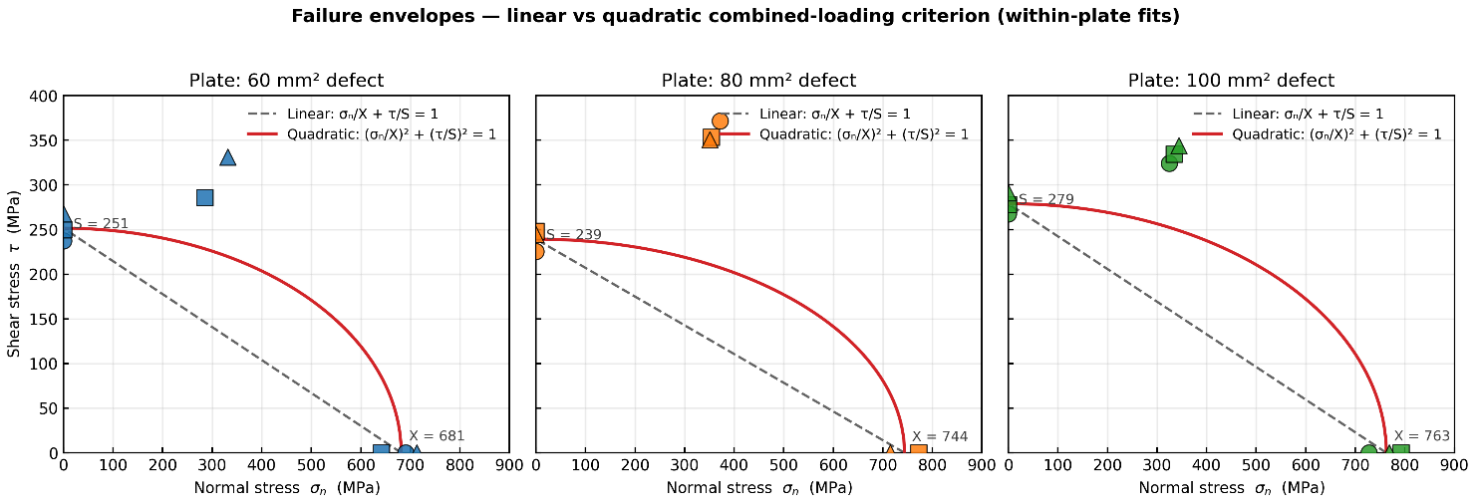


Figure 3

Failure envelope of GFRP butterfly specimens under modified Arcan loading, with linear (Mohr–Coulomb) and quadratic (Tsai–Hill) envelopes anchored at the pure-mode endpoints, shown for each defect plate.

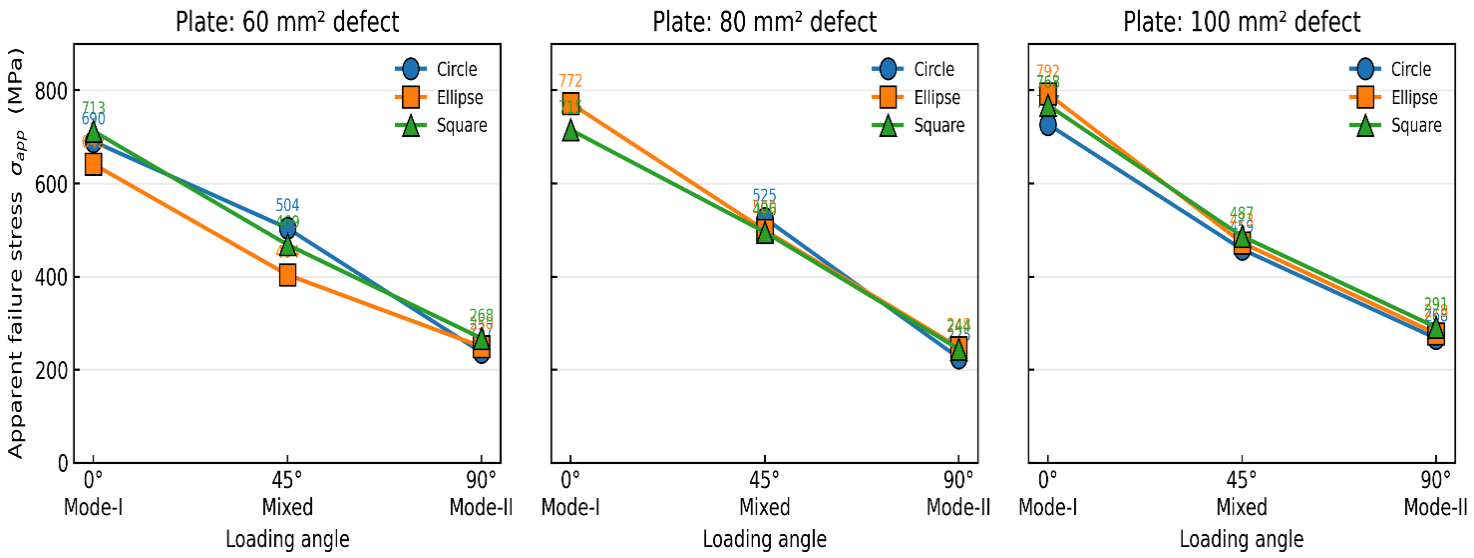


Figure 4

Apparent failure stress against loading angle, within each defect plate. Lines connect specimens of the same defect shape across the three loading angles.

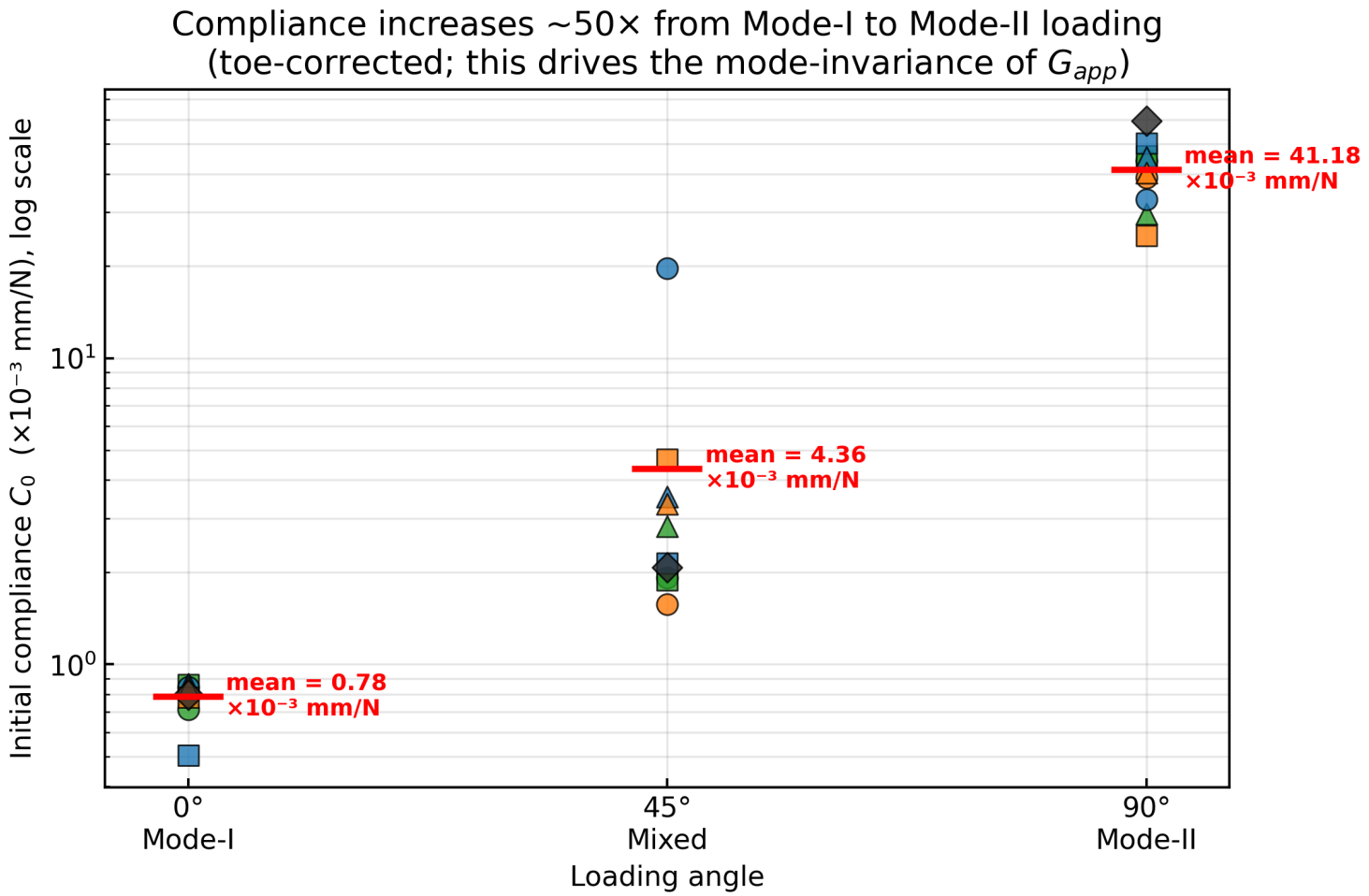


Figure 5

Initial compliance C_0 against loading angle (log scale). Mean values per angle are shown by red horizontal bars.

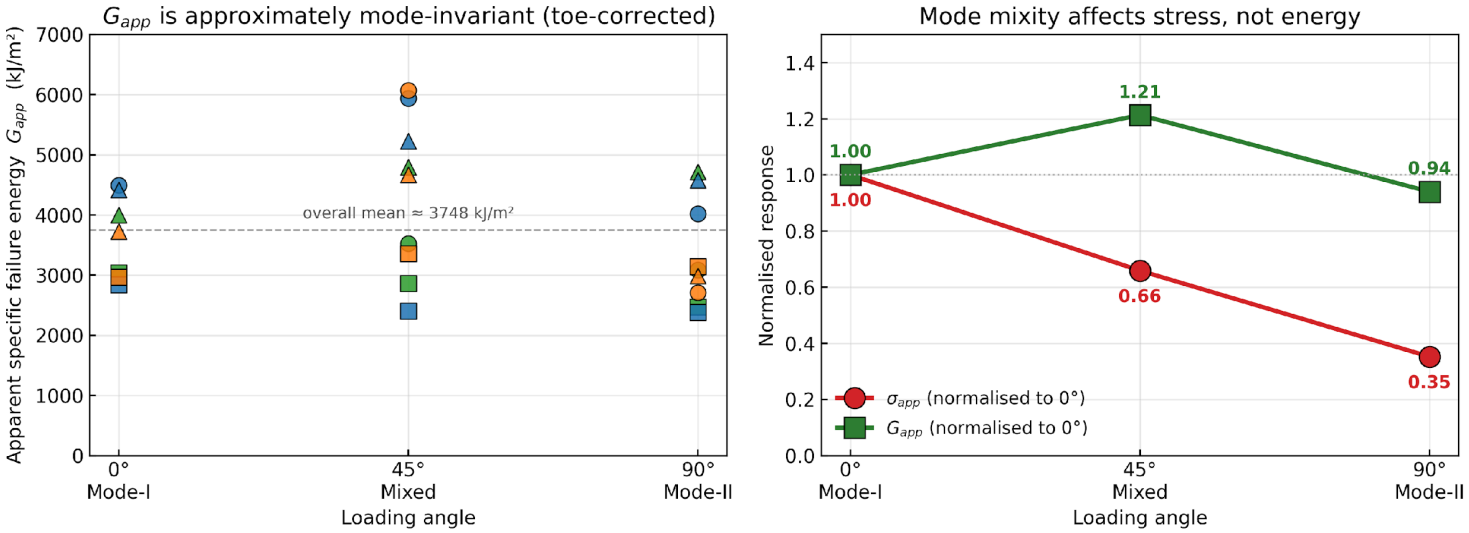


Figure 6

(Left) Apparent specific failure energy Gapp for all defect specimens, by loading angle. (Right) Apparent failure stress σapp and apparent specific failure energy Gapp, normalised to their values at Mode-I, against loading angle.

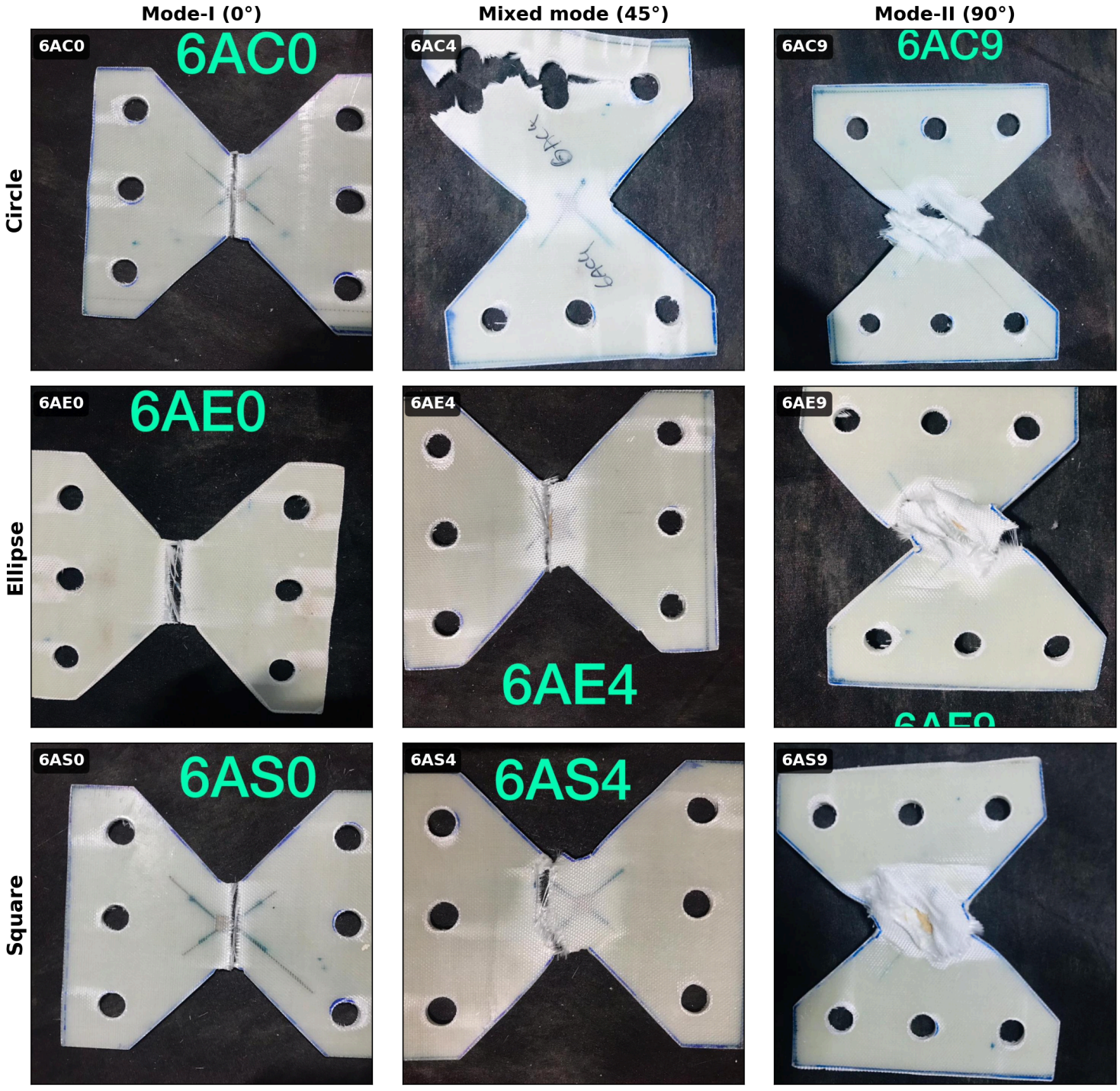


Figure 7

Post-failure photographs of the nine specimens cut from the 60 mm² defect plate. Rows: defect shape (Circle, Ellipse, and Square). Columns: loading angle (Mode-I 0°, mixed 45°, Mode-II 90°). Specimen IDs are shown at the top-left of each panel.